Experimental Heat Transfer
Publication details, including instructions for authors and subscription information:
http://www.informaworld.com/smpp/title~content=t713770473

A HOLOGRAPHIC INTERFEROMETRY STUDY OF THE DOUBLE-DIFFUSIVE LAYERED SYSTEM

Yau-Ming Chen [a]; Chun-Kai Liu [a]
[a] Department of Mechanical Engineering, National Taiwan University, Taipei, Taiwan, Republic of China

Online Publication Date: 01 January 1997

To cite this Article Chen, Yau-Ming and Liu, Chun-Kai(1997)'A HOLOGRAPHIC INTERFEROMETRY STUDY OF THE DOUBLE-DIFFUSIVE LAYERED SYSTEM',Experimental Heat Transfer,10:1,67 — 86
To link to this Article: DOI: 10.1080/08916159708946535
URL: http://dx.doi.org/10.1080/08916159708946535

A HOLOGRAPHIC INTERFEROMETRY STUDY OF THE DOUBLE-DIFFUSIVE LAYERED SYSTEM

Yau-Ming Chen and Chun-Kai Liu
Department of Mechanical Engineering, National Taiwan University, Taipei, Taiwan, Republic of China

This study investigates double-diffusive convection in a two-layer, salt-stratified solution destablized by lateral heating and cooling. The two-wavelength holographic interferometry method was used to measure the transient temperature, concentration, and density distributions. The evolution of the two-layered system can be divided into three stages. In the first stage, the thermally driven convective layers form rapidly, and the existing diffusion layer adjusts itself into a thin interface by convection motion. In the second stage, a quasi-steady state is attained. The temperature distribution is S-type and the temperature difference across the diffusion region does not change much. The concentration distribution is uniform in the two fluid layers, but the concentration and density differences decrease linearly with time. When the interface becomes very thin, unstable finger-type convection appears. Finally, the interface is destroyed by the boundary layers at the side walls in the third stage. The interfacial Nusselt number and Sherwood number are found to increase with the thermal Rayleigh number, and the effect of the solutal Rayleigh number seems to be less significant. The dimensionless mixing time is found to correlate well with thermal and solutal Rayleigh numbers. Results from numerical simulation are demonstrated and compared with the experiments.

Double-diffusive convection occurs in fluids when the density variation is attributed to two different components of molecular diffusivity, that is, thermal and solutal. Various flow patterns, such as salt finger and diffuse layer structure [1], are found in the double-diffusive system. They are influenced by the orientations of temperature and concentration gradients, as described by Ostrach [2].

Double-diffusive layered systems can be seen in many engineering applications, such as solar ponds, liquefied natural gas (LNG) systems, and some energy storage systems [1, 2]. They can also be found in the melts of alloy solidification [3, 4] and crystal growth [5]. Much literature has been devoted to investigation of the onset of cell generation instability and the overall behavior of a multilayered system [1–7]. It has been noted that the interfaces play important roles in the double-diffusive flow field. Actually, the multilayered system is seen to consist of many two-layered systems. For the sake of understanding the transport behavior at the interface, it is necessary to study the two-layered system throughout.

A simple model consisting of an interface with a sharp concentration difference separating two fluid layers and with lateral heating and cooling (see Figure 1)

Received; accepted 20 September 1996.
This research was supported by the National Science Council of the Republic of China through Grant No. NSC 83-0401-E-002-138.
Address correspondence to Prof. Yau-Ming Chen, Department of Mechanical Engineering, National Taiwan University, Taipei, Taiwan 10764, Republic of China. E-mail: ymchen@cc.ntu.edu.tw

Experimental Heat Transfer, 10:67–86, 1997

0891-6152/97 $12.00 + .00

NOMENCLATURE

A	constant in Sellmeier's equation	y	dimensionless coordinate in the vertical direction
AR	Aspect ratio ($= H/W$)	z	interface thickness, m
C	concentration, wt%	α	thermal conductivity, m^2/s
ΔC	concentration difference ($= C - C_r$), wt%	δ	uncertainty
ΔC_{bulk}	concentration difference in fluid layers ($= C_H - C_L$), wt%	β_C	volumetric coefficient of thermal expansion, 1/K
D	mass diffusion coefficient, m^2/s	β_T	volumetric coefficient of expansion with concentration, $(wt\%)^{-1}$
Fo_m	mixing Fourier number ($= Dt_m/W^2$)	λ	wavelength
L	depth of the cavity, m	λ_0	constant in Sellmeier's equation
Le	Lewis number ($= \nu/D$)	ν	kinetic viscosity, m^2/s
N	fringe order	ρ	density, kg/m^3
Nu	Nusselt number ($= dT/dz\|_{cen}\, W/\Delta T_w$)	τ	dimensionless time ($= t\alpha/W^2$)
Pr	Prandtl number ($= \nu/\alpha$)		
$R(\lambda)$	specific refractivity	**Subscripts**	
Ra_T	thermal Rayleigh number ($= g\beta_T \Delta T W^3/\alpha\nu$)		
Ra_S	solutal Rayleigh number ($= g\beta_C \Delta C W^3/\alpha\nu$)	Ar	denoting argon
R_ρ	buoyancy ratio ($= Ra_C/Ra_T$)	bulk	bulk property in fluid layer
S	scalar field	cen	vertical central line
Sh	Sherwood number ($= dC/dz\|_{cen}\, W/\Delta C_{bulk}$)	H	high
t	time, s	He-Ne	denoting helium-neon
t_m	mixing time, s	i	initial state
ΔT	temperature difference ($= T - T_r$)	int	interface
W	width of the cavity, m	j	denoting a wavelength
x	dimensionless coordinate in the horizontal direction	k	denoting a wavelength
		L	low
		r	reference state
		w	wall

has received much research attention. Wirtz and Reddy [8] studied the thermal and solutal fluxes across the interface of a two-layered system experimentally. In thier study, the salinity was measured using a transverse-mounted conductivity probe. They presented correlations for the interfacial thermal and solutal fluxes and tried to extend the results to a multilayered system, but without advanced evidence. Writz [9] examined the interface stability numerically. Bergman and Ungan [10] and Kamakura and Ozoe [11] described comprehensively the evolution of interface degrading and merging by means of flow visualization with liquid crystal and the shadowgraph method, and presented the averaged Sherwood number across the interface by different methods. Bergman and Ungan [10] calculated the solutal driving force of averaged Sherwood number by means of the initial concentration difference in a fluid layer. Kamakura and Ozoe [11] calculated the solutal driving force by measuring the variation of concentration in a fluid layer with respect to time. However, these values were averaged quantities. Literature on the interfacial heat and mass transfer adjacent to the interface is still lacking. Bergman and Ungan [10] also studied the effects of parameters on the mixing time. They found that the mixing time decreases with increasing thermal Rayleigh number and increases with increasing solutal Rayleigh number. Paul and Bergman [12] studied

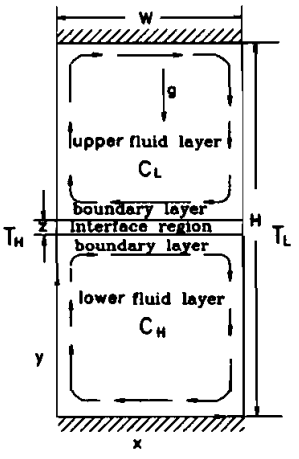

Figure 1. Schematic of lateral heated two-layered convection.

experimentally the concentration variation in the fluid layer using a polarigraphy method. Tanasawa [13] conducted experiments under a constant heat flux condition, to investigate the breakdown of the interface. Recently, Hyun and Bergman [14] simulated a two-layered system numerically. They showed that the averaged Nusselt number fluctuates with respect to time, and the parametric study of mixing time is qualitatively in agreement with the experimental study [10]. Very recently, Kamakura and Ozoe [15] studied numerically the effects of the temperature dependence of properties on the interface migration.

Various techniques have been used in measuring the temperature and concentration in binary-component systems. Intrusive methods are most commonly used, although they disturb the fluid field and are limited to measuring certain fixed points only. Nonintrusive methods, such as the shadowgraph method or polarigraphy, are mostly qualitative in nature or limited to measuring either temperature or the concentration field. However, the double-diffusive convection system is characterized by simultaneous variations in concentration and temperature. To avoid the disadvantages of intrusive methods and to obtain the whole field of transient temperature and concentration data simultaneously, it is believed that the two-wavelength holographic interferometry method is a very promising method. Grob and Wakil [16] used two-wavelength interferometry in a modified Mach-Zehnder interferometer to measure Fick's binary diffusion coefficient in a mixture of gases. Mayinger and Panknin [17] applied two-wavelength holographic interferometry for the measurement of combined heat and mass transfer. Later, some articles used this method to study the transport phenomenon in gaseous systems [18] and alloy solidification [19, 20]. Methea [21] and Worek and Lu [22] investigated the two-wavelength technique for simultaneous temperature and concentration measurements in liquids. Recently, Zheng and Worek [23] used a holographic interferometer to investigate the combined heat and mass transfer process from flowing liquid films. Although this technique has a lot of potential, related studies are still limited.

The above literature survey suggests the use of two-wavelength holographic interferometry for the study of a double-diffusive two-layered system. Therefore, it was applied to measure the temperature and concentration distributions in the present study. The working medium used in the experiments is NaCl–H_2O. Focus was on the transient heat and mass transfer across the interface and how they affect the interface degrading and merging. Parametric study was carried out, and the experimental results were compared with those from numerical simulation.

EXPERIMENTAL TECHNIQUES

Experimental Setup

The experiments were conducted in a rectangular cell whose top, base, front, and back were made of acrylic, while the side walls consisted of 5-mm-thick copper plates with circulating passages at back. The test cell consisted of a deep rectangular enclosure 80 mm high × 40 mm wide × 30 mm. The bottom and top walls each had a drilled and tapped hole in the center for filling and drawing-out purposes. Holes on the top walls were also provided to allow access for the thermocouples and concentration measurements. Four T-type thermocouples were embedded in each side wall to measure the surface temperature of the copper plates, and a Yokogawa HR-2500 data acquisition system was used to record all thermocouple readings. Two constant-temperature recirculating-bath refrigerators with a PID controller were used to maintain the predetermined temperatures. Initial concentration of the salt–water system was prepared by high-precision scale.

A schematic of the two-wavelength holographic interferometry is shown in Figure 2. The light sources used were a 40-mW He-Ne laser ($\lambda_{He\text{-}Ne}$ = 632.8 nm) and a 2-W argon laser (λ_{Ar} = 514.5 nm). Each laser beam was spatially filtered and collimated separately. By using a 50-mm-cube beam splitter, the input laser beams were divided into a reference and an object beam. Due to the two different wavelengths, two kinds of holographic plates, Agfa 10E75 and Agfa 10E56, were

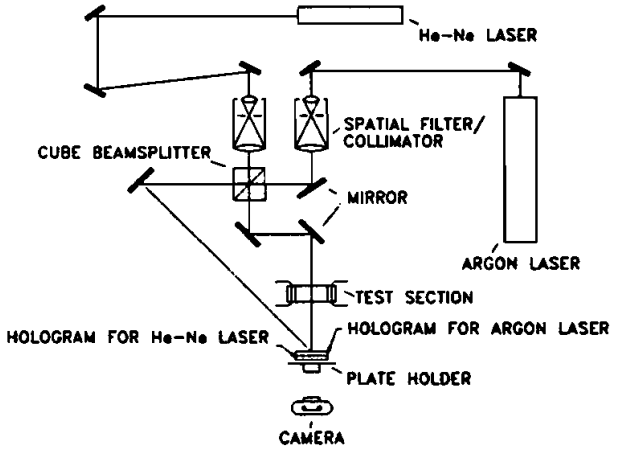

Figure 2. Schematic of the experimental setup for holographic interferometry.

used for the He-Ne laser and the argon laser, separately. A sandwich hologram approach was adopted, as illustrated in Figure 2, and the optimal exposure time for both holographic plates was found by trial and error. After the exposure, both holographic plates were developed and bleached. In this study, a real-time technique was used, in which a uniform refractive index field was recorded as a reference. After processing the two holograms chemically, each could be reconstructed separately. This was done by illuminating the hologram plates with the reference beam while the other laser beams of different wavelengths were blocked. Now, the experiments could be started and the interferometric fringe patterns were recorded with a Nikon FM-2 camera using Agfa AP × 25 film. The entire holographic interferometer together with the test section was mounted on an antivibration optical table.

The procedure for running the experiments was as follows. To set up the initial condition, the lighter $NaCl-H_2O$ was gradually poured by the tubing pump into the test section, which had been half-filled with heavier $NaCl-H_2O$. Thus, a two-layered system was prepared. After developing the holograms, the two constant-temperature baths to heat and cool the side walls were started, and the circulating fluids ran separately through the heat transfer passages. Note that the circulating fluids had already been set to the predetermined temperatures. Two separate sets of interferometry fringe pattern were recorded alternatively by camera until the end of the experiment. To perform the interferometric measurements, the interferograms obtained were analyzed with the aid of an optical profile projector (Mitutoyo PJ311) with 1-μm resolution.

Procedure for Two-Wavelength Interferometry Data Processing

For the two-wavelength technique, the experimental setup is more complex and the interferometry fringe analysis is more difficult than for the single-wavelength technique. A detailed introduction to the holographic interferometry method can be found in [17, 24]. The single-wavelength technique measures the fringe shift N in a transparent medium and uses the following equation to evaluate the scalar field S:

$$S = S_0 + \left(\frac{1}{\partial n/\partial S}\right)\left(\frac{\lambda N}{L}\right) \tag{1}$$

where $\partial n/\partial S$ is the refractive index variation with the scalar, λ is the source wavelength, N is the fringe order, L is the depth of the test section, and S_0 is the reference value of the scalar field. If the scalar field includes temperature T and concentration C, then Eq. (1) can be modified to yield both the scalars by solving the following equations simultaneously:

$$\frac{N_j\lambda_j}{L} = \left(\frac{\partial n}{\partial C}\right)_j \Delta C + \left(\frac{\partial n}{\partial T}\right)_j \Delta T \tag{2}$$

$$\frac{N_k\lambda_k}{L} = \left(\frac{\partial n}{\partial C}\right)_k \Delta C + \left(\frac{\partial n}{\partial T}\right)_k \Delta T \tag{3}$$

In the above equations, the subscripts j and k refer to two different source wavelengths λ_j and λ_k. ΔT and ΔC are temperature and concentration differentials above T_r and C_r, respectively. These equations make use of the fact that, in addition to density, the refractive index of a transparent medium is also a function of the source wavelength. Solving eqs. (2) and (3) yields Eqs. (4) and (5):

$$\Delta T = \Delta N_j \left[\frac{\lambda_k (\partial n/\partial C)_j}{D} \left(\frac{\Delta N_k}{\Delta N_j} \right) - \frac{\lambda_j (\partial n/\partial C)_k}{D} \right] \tag{4}$$

$$\Delta C = \left[\frac{\lambda_j}{L} \Delta N_j - \left(\frac{\partial n}{\partial T} \right)_j \Delta T \right] \Big/ \left(\frac{\partial n}{\partial C} \right)_j \tag{5}$$

where

$$D = \left(\frac{\partial n}{\partial T} \right)_k \left(\frac{\partial n}{\partial C} \right)_j - \left(\frac{\partial n}{\partial T} \right)_j \left(\frac{\partial n}{\partial C} \right)_k \tag{6}$$

Note that the ΔN_j and ΔN_k are obtained from the reconstructed holograms. To calculate the values of $(\partial n/\partial C)_{j,k}$ and $(\partial n/\partial T)_{j,k}$, the relations between the refractive index, concentration, and temperature should be known first. After a thorough search, we were unable to locate this information directly in the open literature. Fortunately, there does exist some very useful information. Metha and Worek [25] presented the relations for wavelengths of 486.1 nm and 656.3 nm, and although they are different from the wavelengths used in our study, i.e., 632.8 nm (He-Ne laser) and 514.5 nm (argon laser), useful information can still be derived. By means of Sellmeier's formula,

$$n^2 - 1 = \frac{A\lambda^2}{\lambda^2 - \lambda_0^2} \tag{7}$$

we were able to calculate the two constants, A and λ_0, from the relations obtained for wavelengths of 486.1 nm and 656.3 nm in [25]. With this information, the refractive index at different wavelengths could then be deduced from Eq. (7). The relations between the refractive index at different temperatures and concentrations were obtained. After using a curve-fitting procedure involving a linear equation with two variants, the results are as follows:

$$n_{\text{He-Ne}}(C,T) = 1.3336 - 1.0725 \times 10^{-4} T + 1.71 \times 10^{-3} C \tag{8}$$

$$n_{\text{Ar}}(C,T) = 1.3383 - 1.1199 \times 10^{-4} T + 1.7531 \times 10^{-3} C \tag{9}$$

The standard deviations for the above equations are 5.09×10^{-5} and 4.97×10^{-5}, respectively. The maximum difference between the value calculated from Eq. (8) and that of Worek and Lu [26] is smaller than 0.001 in the temperature and concentration ranges of this study. Equation (7) can be calculated from Eqs. (8) and (9), and the distributions of temperature and concentration in the whole flow field can be obtained using Eqs. (4) and (5).

In addition to the temperature and concentration fields, the density distributions can also be deduced using holographic interferometry. For fluids, the Lorentz-Lorenz equation gives the relation between the refractive index n and the density ρ:

$$\frac{n^2(T,C)-1}{n^2(T,C)+2} = R(\lambda)\rho(T,C) \tag{10}$$

where $R(\lambda)$ is the specific refractivity. By using the relationship of density, temperature, and concentration in Ruddick and Shirtcliffe [27] together with the relations (8) and (9), $R(\lambda)$ at different wavelengths can be obtained. The values are 2.0249×10^{-1} for the He-Ne laser and 2.0509×10^{-1} for the argon laser in a temperature range of 10–30°C and a concentration range of 0–5%, respectively.

From an error analysis presented in [28], it is noted that, in order to reduce possible source of error, the fringe order N must be precisely determined. This also means that the measurement of N in two-wavelength holographic interferometry should be more accurate than in the single wavelength method.

Suppose that the possible error in N is ΔN. The following equations are used to estimate the errors [27]:

$$\delta(\Delta T) = \pm\delta(\Delta N)\frac{\left[\lambda_j|(\partial n/\partial C)_k| + \lambda_k|(\partial n/\partial C)_j|\right]}{LD} \tag{11}$$

$$\delta(\Delta C) = \pm\delta(\Delta N)\frac{\left[\lambda_j|(\partial n/\partial T)_k| + \lambda_k|(\partial n/\partial T)_j|\right]}{LD} \tag{12}$$

Here, $\delta(\Delta T)$ and $\delta(\Delta C)$ are the uncertainties as compared to the respective error-free values. There are two errors to be considered: the error associated with the fringe measurements and the error associated with the refractive measurements. With reference to the refractive index measurements, the standard deviation of the refractive-index linear equations from the measured data has already been reported as 5.09×10^{-5} and 4.97×10^{-5}, for the He-Ne and argon equations, respectively. The relative errors in dn/dT and dn/dC can be measured to about 0.01% accuracy. The effects of these errors can thus be neglected. As to the fringe order measurements, the accuracy is estimated to be 1/10. Substituting the relevant values into Eqs. (11) and (12), the uncertainties for temperature and concentration measurements are estimated to be within 16% and 13%, respectively. For better accuracy, temperature measurements can be carried out with thermocouples, while the concentration distribution is measured by means of holographic interferometry. In this way, the uncertainties for the thermocouple measurements and concentration measurements are estimated to be 4% and 6%, respectively.

RESULTS AND DISCUSSION

Flow Evolution of Transport Phenomenon in a Two-Layer System

Prior to imposing the thermal boundary condition, no convection is evident and a thick diffusion layer exists between two fluid layers, as shown in Figure 3*a*.

This is due to the diffusion of concentration from the lower fluid layer. Once the thermal boundary condition is imposed, the thermally driven flow induces convection. The large concentration gradient between the two fluid layers retards the flow motion in a vertical direction and creates two circulations. In Figure 3*b*, it is shown that the flow along the side walls comes into collision with the diffusion layer, leading to two denser lines above and below the diffusion layer. These two lines can also be seen in shadowgraph results [11]. From the interferometry fringes, the detailed structure can be seen more clearly. The diffuse layer is diminished immediately and the weak intermediate layer appears in the middle region due to the shear forces above and below it. In addition, secondary flow is evident in the upper left and lower right of the interface; see Figure 3*c*. Secondary flow was also found by Bergman [10] and Hyun [14]. Because the circulations are not well developed, the unmixed concentration accumulates in the corner of the diffusion layer. When the thermally driven flow is fully developed, the two circulations compress the diffuse layer to a thin interface, as shown in Figure 3*d*. The time for this to happen is at about 15 min.

Two circulations with a sharp interface make up the two-layered system. Because the thermal diffusivity is much larger than the solutal diffusivity (Le $\approx$ 100), the temperature field reaches a stable state sooner, but the concentration is still transferred from the lower fluid layer. Due to mass transfer, the interface becomes thinner and thinner. The interferometric fringes do not change much at the fluid layers but decrease at the interface during this time, as shown in Figure 3*e*, which can be seen as a quasi-steady state [8]. The velocity, thermal, and solutal boundary layers are generated along the interface. These boundary layers dominate the transport phenomenon at the interface. However, the boundary layers along the side walls have direct effects on keeping the interface, as will be discussed later. Because the quasi-steady state remains until the interface starts to break down, it was possible to obtain some important values about the heat and mass transfer of the interface during this time.

When the interface is very thin, it will tilt more due to the boundary-layer flow along the sidewalls, as seen in Figure 3*f*. If the density difference with respect to the shear force comes to a critical value, the Kelvin-Helmholtz instability occurs. Waves form along the interface and the interface twists. Due to the preferential heating of the higher-salinity fluid and the instability of the interface, warm, salty water overlies cool, fresher water. Salt fingers appear at the interface and side walls. The vortices due to salt-finger convection can be seen clearly at the interface. The unstable finger-type convection makes the interferometry fringes somewhat shaky, as shown in Figure 3*g*.

This instability reinforces the transport phenomenon of the interface. The stable salinity interface cannot resist the unstable thermal effects, and the interface breaks down from the side walls by the velocity boundary layer [15]. The breakdown in not symmetrical, and occurs slightly earlier at the heating boundary. This phenomenon may be due to non-Boussinesq behavior [10]. After the interface is entirely gone, a random and vigorous mixing can be seen in the cavity. The time for breakdown of interface is short. Finally, as the merging is completed, the flow field comes into natural convection, as shown in Figure 3*h*.

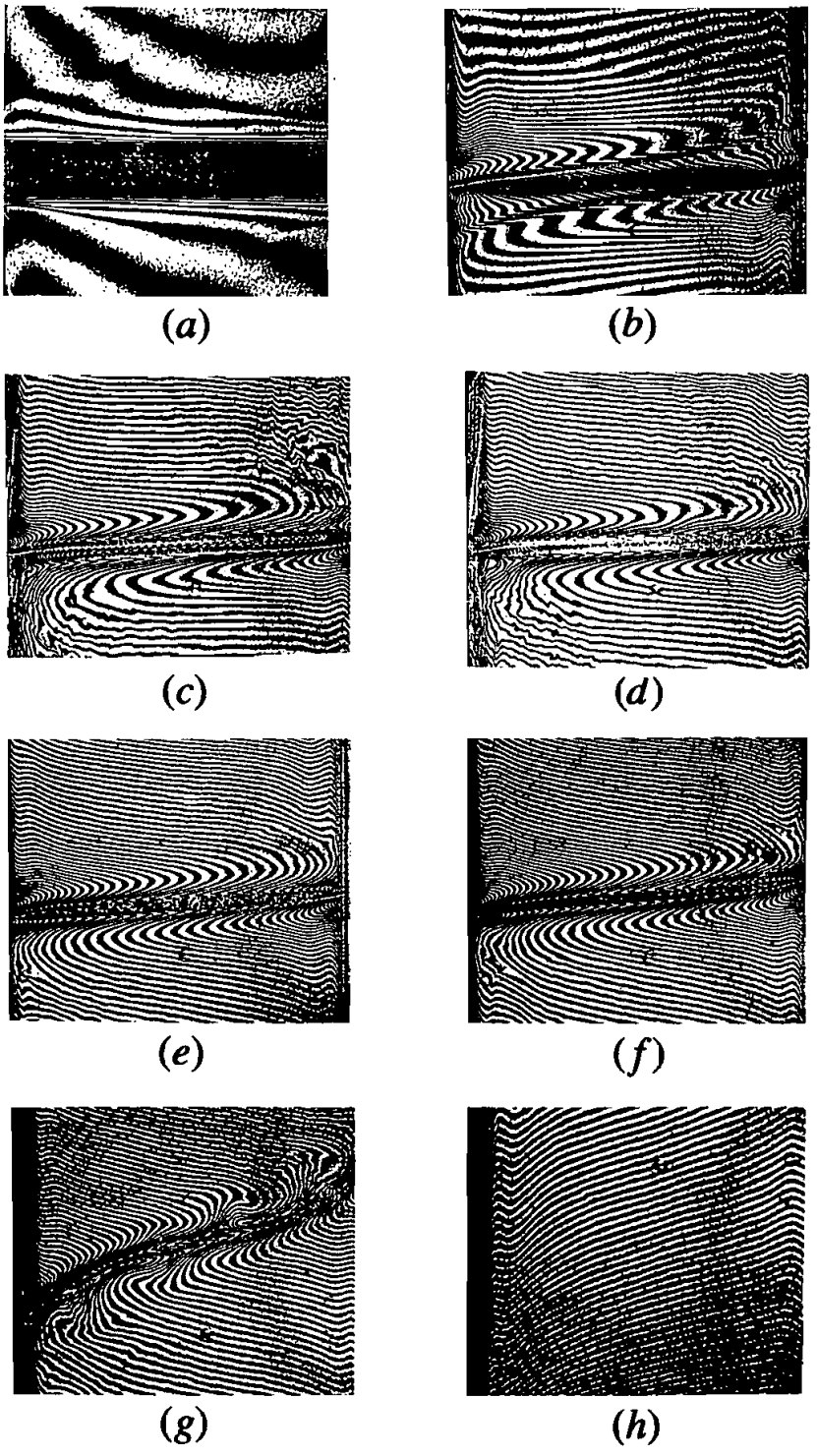

Figure 3. Interferometry fringes for a two layered system at: (*a*) 0 min; (*b*) 2 min; (*c*) 6 min; (*d*) 15 min; (*e*) 30 min; (*f*) 90 min, (*g*) 180 min, (*h*) 200 min.

Temperature, Concentration, and Density Distributions

The interface between the two circulations guides the whole flow evolution. By using the two-wavelength holographic interferometry method, we were able to obtain the temperature and concentration distributions in the whole flow field. Figures 4 and 5 show the vertical temperature and concentration profiles along the midplane at different times. The tendencies are similar to the results of [8] and [11, 12]. However, the data in this study are more complete. From Figures 4 and 5, there are diffusion regions at the middle of the cavity in the vertical direction. The heat and mass are transferred across the interface by diffusion. This is different from the vivid convection phenomenon in the fluid layers. The temperature distribution is *S*-type. This distribution is maintained for a longer time, as shown in Figures 4*b* and 4*c*. When the interface breaks down, the flow field begins to become unstable and the temperature distribution is also twisted, as shown in Figure 4*d*. Finally, it comes to steady state and becomes natural convection in the entire cavity.

Figures 5*a*–5*e* show the concentration distribution at different times. The distribution is uniform at each fluid layer but is linear at the interface. In the beginning, the mass transfer is by diffusion; when the convection is reinforced, the mass transfer becomes stronger and the variation of the concentration gradient at the interface is larger. During the quasi-steady state period, the concentration difference decreases until it becomes uniform at the final steady state.

The density distributions have different forms; see Figures 6*a*–6*e*. They are influenced by the combined effects of temperature and concentration. There are two inversion points adjacent to the interface in the fluid layer. One is at the core region of the temperature boundary layer and the edge of the solutal boundary layer. The other point is very near the interface, as shown in Figure 7, which shows comparable plots of interferometry fringes and the various boundary layers. According to Figure 7, the interfacial thermal and solutal boundary layers are measured about 3–4 mm from the center of the cavity. In addition, the locations of interface move upward during experiments, as described by [11, 15].

Heat and Mass Transfer Rates at the Interface

For discussion of the heat and mass transfer behavior at the interface, the temporal variations in the thickness of interface are shown in Figure 8. The history of the thickness of the interface can be divided into three stages. The first stage is the transformation from a diffusion layer to a thin interface. The thickness reduces abruptly in a short time. At the second stage, the thickness decreases slightly with time. When the interface is very thin and cannot remain as a two-layered structure, it decreases sooner. This is the third stage. The variation of thickness with time at each stage is nearly linear, and the gradient is the same at the same solutal Rayleigh number but increases with the thermal Rayleigh number. The temperature difference in the diffusion region does not change much at the same Ra but decreases as Ra_S increases, as shown in Figure 9. However, the concentration difference of the diffusion region decreases linearly with respect to time, as shown in Figure 10. From Figure 11, it can be seen that the density difference across the

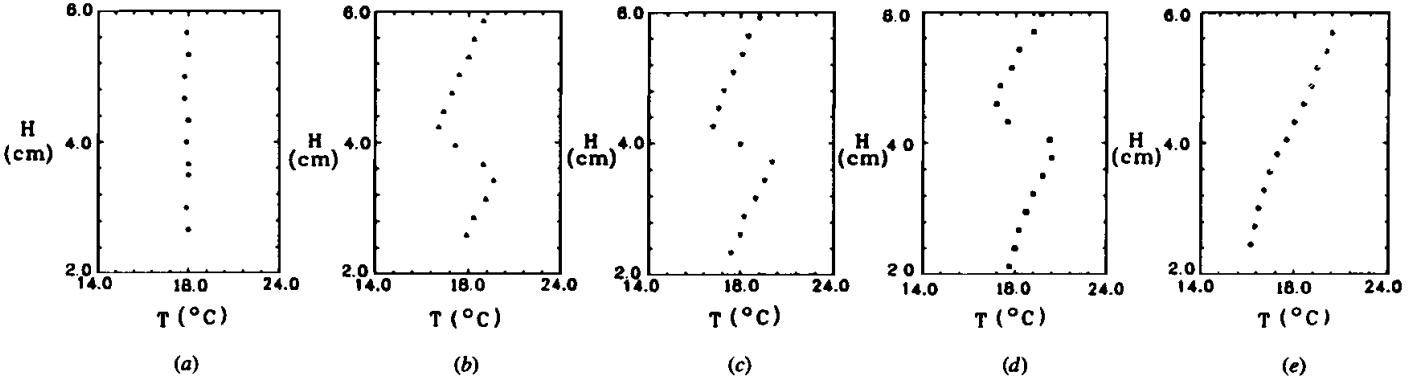

Figure 4. Time history of the temperature profile development in a two-layered system for $Ra_T = 1.1 \times 10^7$, $Ra_S = 1.76 \times 10^7$. Times from left to right are: (*a*) $t = 0$ min; (*b*) $t = 20$ min; (*c*) $t = 90$ min; (*d*) $t = 180$ min; (*e*) $t = 200$ min.

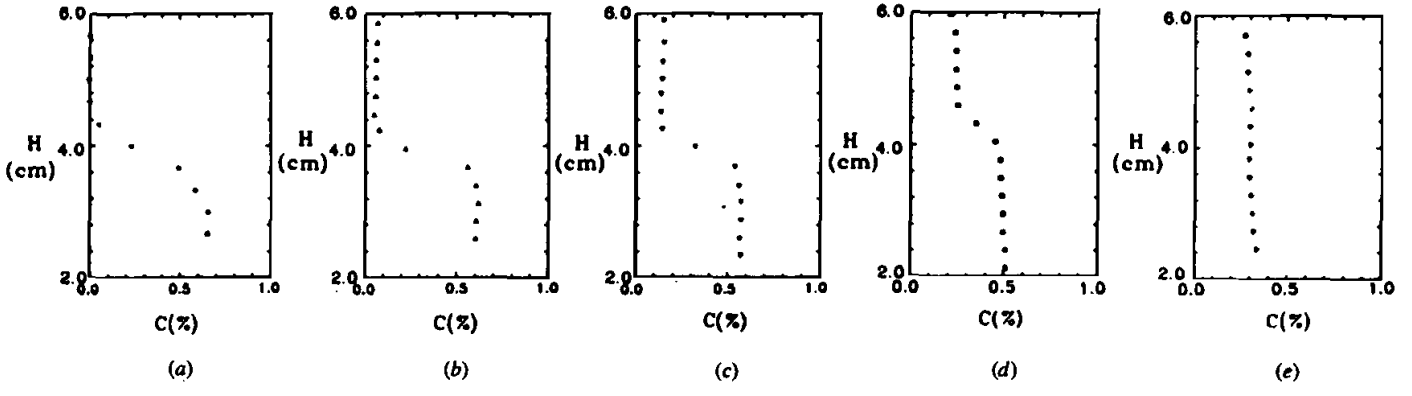

Figure 5. Time history of the concentration profile development in a two-layered system for $Ra_T = 1.1 \times 10^7$, $Ra_S = 1.76 \times 10^7$. Times from left to right are: (*a*) $t = 0$ min; (*b*) $t = 20$ min; (*c*) $t = 90$ min; (*d*) $t = 180$ min; (*e*) $t = 200$ min.

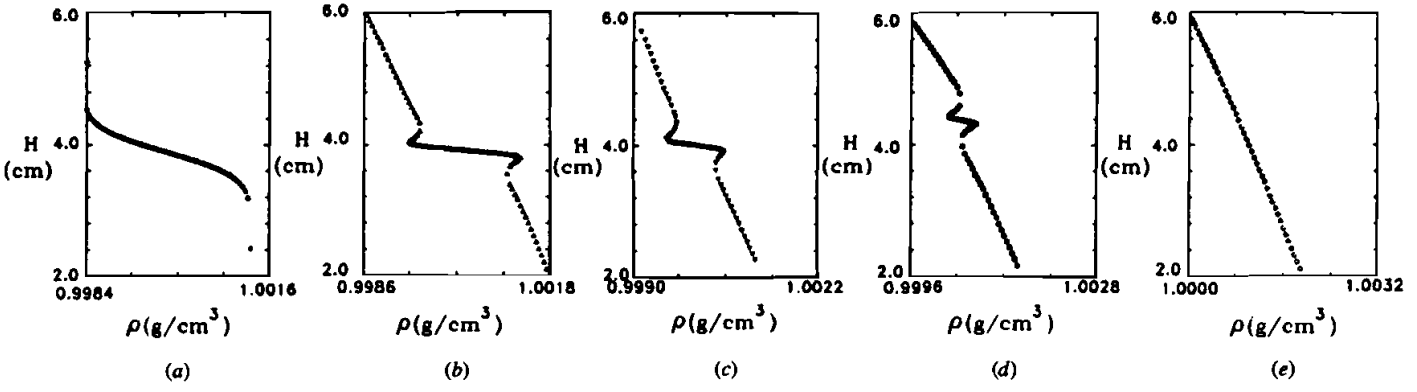

Figure 6. Time history of the density profile development in a two-layered system for $Ra_T = 1.1 \times 10^7$, $Ra_S = 1.76 \times 10^7$. Times from left to right are: (*a*) $t = 0$ min; (*b*) $t = 20$ min; (*c*) $t = 90$ min; (*d*) $t = 180$ min; (*e*) $t = 200$ min.

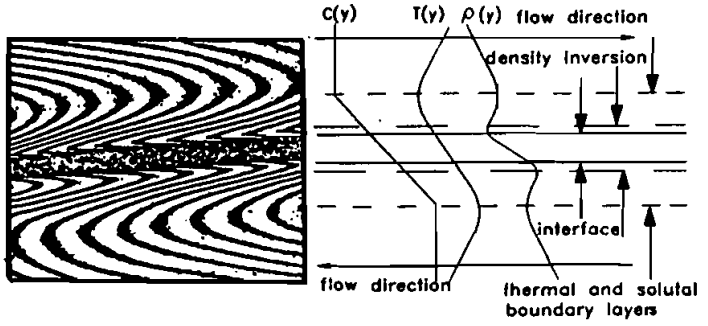

Figure 7. Schematic of the transport phenomena adjacent to the interface.

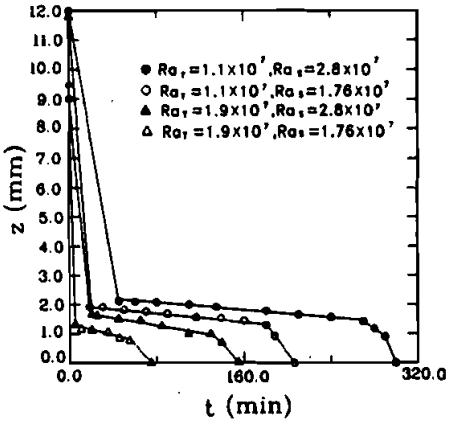

Figure 8. Time history of the interface thickness in a two-layered system.

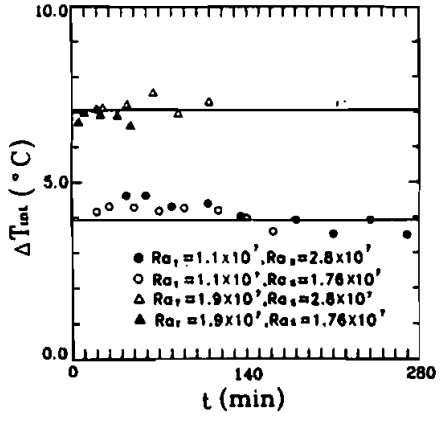

Figure 9. Time history of temperature difference across the interface.

interface also decreases linearly with time. The rate of concentration difference across the diffusion region and the density difference across the interface with respect to time increase with Ra, but are independent of Ra_S, as shown in Figures 10 and 11.

As mentioned before, the heat and mass transfer across the interface are measured by holographic interferometry, which is different from the methods used in [10] and [11]. In these articles, the solutal driving force of averaged Sherwood number from the concentration difference in the fluid layer was estimated. The interfacial Nusselt number and the Sherwood number are defined as

$$\mathrm{Nu} = \frac{(dT/dL)|_{\mathrm{cen}} W}{\Delta T_w} \tag{13}$$

$$\mathrm{Sh} = \frac{(dC/dL)|_{\mathrm{cen}} W}{\Delta C_{\mathrm{bulk}}} \tag{14}$$

where ΔT_w is the temperature difference between the side walls and ΔC_{bulk} is the concentration difference between the upper and lower fluid layers.

The results of averaged Nusselt number and Sherwood number obtained during the quasi-steady-state period are listed in Table 1, where it is shown that the Nusselt number increases with thermal Rayleigh number but decreases slightly with solutal Rayleigh number. This is because the thermal driving force enhances the interfacial heat transfer rate, but the solutal driving force has the opposite effect. On the other hand, it is interesting that the variation in Sherwood number is similar to the variation in Nusselt number. These similar variations for thermal and solutal transfer coefficients can be found in many binary systems [20, 23].

Mixing Time

The merging of the interface is affected by the properties of the working medium, the aspect ratio, the velocity boundary layer at the side walls, and the heat and mass transfer of the interface. Because the parameters Pr and Le are fixed, the

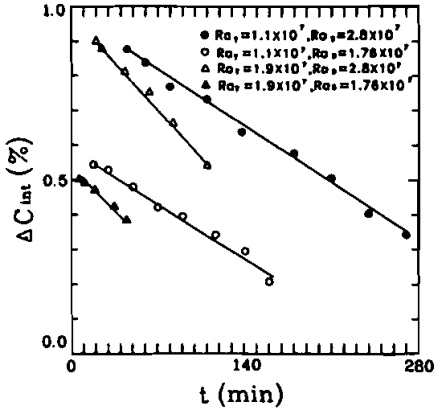

Figure 10. Time history of concentration difference across the interface.

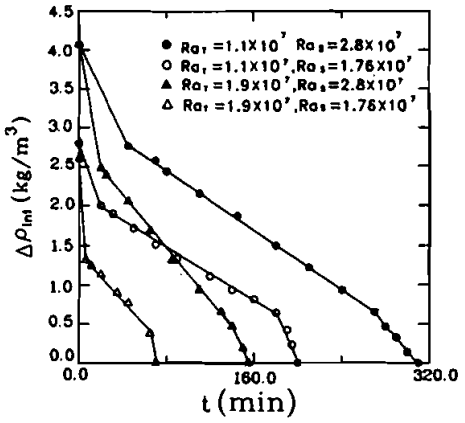

Figure 11. Time history of density difference across the interface.

whole process is related to the other parameters, i.e., thermal Rayleigh number, solutal Rayleigh number, and aspect ratio. Here only the first two parameters are discussed, while the aspect ratio is fixed at 2 in this study. From the experimental results, the correlation of the dimensionless mixing time in terms of thermal Rayleigh number and buoyancy ratio is developed and can be expressed as

$$\mathrm{Fo}_m = 14.8\,\mathrm{Ra}_T^{-0.4912}\,R_\rho^{1.6} \tag{15}$$

The results are shown in Figure 12. The inaccuracy of t_m is about ± 60 s, and thus the error of Fo_m is estimated to be within $\pm 5\%$. It is noted that the dimensionless mixing time increases as the initial buoyancy ratio R_ρ increases, but decreases as Ra_T increases. When Ra_T increases, the interfacial heat transfer and fluid motion along the side walls are also stronger and are able to destroy the interface more easily. In addition, although ΔC increases with ΔT for the same R_ρ, the thermal effect reinforces the convection in the two fluid layers and then enhances the mass transfer through the interface and offsets the increase in Fo_m associated with larger ΔC. Therefore, the parameter R_ρ has a stronger influence than Ra_S on the mixing time.

Comparison with Numerical Simulation

For comparison, numerical simulations were also carried out. The governing equations were discretized by using a weighting function [29]. In addition, an APPLE algorithm was adopted to deal with the Navier-Stokes equations [30]. It was noted that a proper initial concentration distribution and suitably fine grids at the interface are important. Hyun and Bergman [14] simulated the distribution by an error function obtained from the solution of one-dimensional, transient mass transfer equation. Here in this study, the initial condition was given by fitting the results from holographic measurements with an error function. The grid meshes were concentrated at the boundaries and interface, due to the thermal and solutal boundary layers and complex transport behavior there. If there are not enough grid

Table 1. Interfacial Sherwood number and Nusselt number for different thermal and solutal Rayleigh numbers

	Sh	Nu
$Ra_T = 1.1 \times 10^7$ $Ra_S = 1.76 \times 10^7$	6.	3.29
$Ra_T = 1.1 \times 10^7$ $Ra_S = 2.8 \times 10^7$	5.78	3.11
$Ra_T = 1.9 \times 10^7$ $Ra_S = 1.76 \times 10^7$	11.45	5.67
$Ra_T = 1.9 \times 10^7$ $Ra_S = 2.8 \times 10^7$	9.33	4.73

nodes near the interface, the predicted evolution of interface will occur sooner. After some tests for grid independence, grid meshes of 80×300 were adopted. Similar methods were adopted in the double-diffusive multilayered system [28]. Figure 13 shows, as an example, the computed results of the refractive index field at $Ra_T = 1.1 \times 10^7$, $Ra_S = 1.76 \times 10^7$, and AR = 2. Figures 13*a* and 13*b* are at the first stage. They are similar to the results of Figures 3*b* and 3*c*. Similarly, Figures 13*c* and 13*d* are at the second and third stages, and they are similar to Figures 3*e* and 3*g*, separately. Comparison shows that the interferometric and numerical results agree at different time stages.

CONCLUSION

An experimental study of a two-layered, salt-stratified system that is destabilized by lateral heating and cooling was carried out. The two-wavelength holographic interferometry method was used to measure the temperature, concentration, and density distributions. The major conclusions are as follows.

1. The evolution of two-layered systems can be divided into three stages, and for each stage there are different characteristics. In the first and shortest stage, the diffusion layer reduces abruptly and two circulations appear. The secondary flow

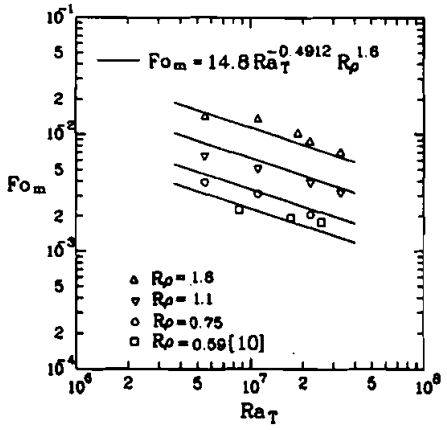

Figure 12. Correlation of the dimensionless mixing time.

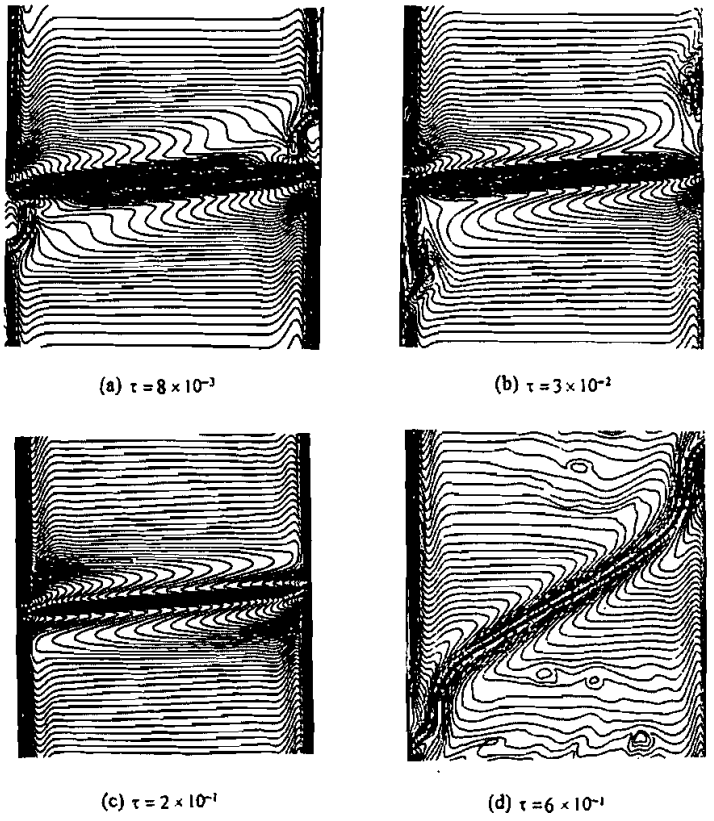

Figure 13. Numerical simulation of the refractive index field for $Ra_T = 1.1 \times 10^7$, $Ra_S = 1.76 \times 10^7$ at different times.

and intermediate layer can be seen in this stage. The quasisteady state is maintained in the second stage, which is the longest. In this stage the temperature distribution does not change much, but the concentration decreases. The layer breaks down in the third stage. The breakdown of the interface is generated from the boundaries, due to the strong boundary layer at the side walls. Vivid salt-finger convection can be seen in this stage. After the interface breaks down, the flow field experiences random mixing and finally comes to a steady state.

2. At the quasi-steady state, the temperature difference in the diffusion region does not change much. However, the concentration difference in the diffusion region and the density difference across the interface decrease linearly with respect to time. In addition, the layer thickness also decreases linearly with time. The thermal effect is unstable and the solutal effect is stable for the flow field. The flow motion is induced by thermal effects, but the interface degradation is generated by solutal effects. From the results of interfacial heat and mass transfer coefficients, it is shown that the averaged Nusselt number and averaged Sherwood numbers increase with thermal Rayleigh number but decrease with solutal Rayleigh number. Thus, thermal effects are more significant than solutal effects.

3. The dimensionless mixing time of a two-layered system can be correlated with respect to the parameters of thermal Rayleigh number and buoyancy ratio. The mixing time increases with thermal Rayleigh number but decreases with buoyancy ratio. Thus, thermal Rayleigh number has more striking effects for layer mixing.

4. Comparison between experimental and numerical simulations shows close agreement at different time stages.

REFERENCES

1. J. S. Turner, *Buoyancy Effects in Fluids*, Cambridge University Press, London, 1973.
2. S. Ostrach, Natural Convection with Combined Driving Forces, *PhysicoChem. Hydrodyn.*, vol. 1, pp. 233–247, 1980.
3. M. E. Thompson and J. Szekely, Density Stratification due to Counterbuoyant Flow along a Vertical Crystallization Front, *Int. J. Heat Mass Transfer*, vol. 32, pp. 1021–1036, 1989.
4. J. Tanny, Experimental Study on the Crystallization of a Binary Melt at the Vertical Boundary of an Enclosure, *Int. J. Heat Mass Transfer*, vol. 37, pp. 1141–1150, 1994.
5. S. Ostrach, Fluid Mechanics in Crystal Growth—The 1982 Freeman Scholar Lecture, *J. Fluids Eng.*, vol. 105, pp. 2–20, 1982.
6. C. F. Chen, D. G. Briggs, and R. A. Writz, Stability of Thermal Convection in a Salinity Gradient due to Lateral Heating, *Int. J. Heat Mass Transfer*, vol. 14, pp. 57–65, 1971.
7. J. Tanny and A. B. Tsinober, The Dynamics and Structure of Double-Diffusive Layers in Sidewall-Heating Experiments, *J. Fluid Mech.*, vol. 196, pp. 135–156, 1988.
8. R. A. Writz and C. S. Reddy, Heat and Mass Transport across Diffusive Interfaces Bounded by Turbulent Convecting Regions, *Int. J. Heat Mass Transfer*, vol. 19, pp. 471–478, 1976.
9. R. A. Writz, The Effect of Solute Layering on Lateral Heat Transfer in an Enclosure, *Int. J. Heat Mass Transfer*, vol. 20, pp. 841–846, 1977.
10. T. L. Bergman and A. Ungan, A Note on Lateral Heating in a Double-Diffusive System, *J. Fluid Mech.*, vol. 194, pp. 175–186, 1988.
11. K. Kamakura and H. Ozeo, Double-Diffusive Convection between Vertical Parallel Walls—Experimental Study of Two-Layer Convection, *J. Chem. Eng. Jpn.*, vol. 24, pp. 622–627, 1991.
12. I. Tanasawa, Experimental Techniques in Natural Convection, *Exp. Thermal Fluid Sci.*, vol. 10, pp. 503–518, 1995.
13. T. H. Paul and T. L. Bergman, Polarigraphic Measurement of Liquid-Phase Species Distributions, *Exp. Thermal and Fluid Sci.*, vol. 10, pp. 519–524, 1995.
14. M. T. Hyun and T. L. Bergman, Direct Simulation of Double-Diffusive Layered Convection, *J. Heat Transfer*, vol. 117. pp. 334–339, 1995.
15. K. Kamakura and H. Ozoe, Effect of the Temperature Dependence of Fluid Properties on the Migration of an Interface in Double-Diffusive Natural Convection, *Int. J. Heat Mass Transfer*, vol. 38, pp. 3413–3421, 1995.
16. A. K. Grob and M. M. El-Wakil, An Interferometric Technique for Measuring Binary Diffusion Coefficients, *J. Heat Transfer*, vol. 96. pp. 259–266, 1969.
17. F. Mayinger and W. Panknin, Holography in Heat and Mass Transfer, *Proc. 5th Int. Heat Transfer Conf.*, Tokyo, Japan, pp. 28–43, 1974.
18. M. M. El-Wakil and C. L. Jaeck, A Two-Wavelength Interferometer for the Study of Heat and Mass Transfer, *Trans. ASME*, vol. 32. pp. 464–466, 1964.
19. A. Eckert, Two Wavelength Holographic Measurement of Temperature and Concentration during Alloy Solidification, *J. Thermophys. Heat Transfer*, vol. 2, pp. 193–196, 1988.

20. T. L. Spatz, A Holographic Interferometry Study on the Freezing of an Alloy around a Pipe in the Presence of a Mixed Phase Region, Ph.D. dissertation, University of Illinois at Chicago, 1992.
21. J. M. Metha, Experimental and Analytical Investigation of a Thermo-haline, Double-Diffusive System, Ph.D. dissertation, Illinois Institute of Technology, 1985.
22. W. M. Worek and W. Lu, Measurement Errors Associated with Two-Wavelength Interferometric Techniques in Salt Water Solutions, *Int. Commun. Heat Mass Transfer*, vol. 21, pp. 1–8, 1994.
23. G. S. Zheng and W. M. Worek, Method of Heat and Mass Transfer Enhancement in Film Evaporation, *Int. J. Heat Mass Transfer*, vol. 39, pp. 97–108, 1996.
24. C. M. Vest, *Holographic Interferometry*, John Wiley, New York, 1979.
25. J. M. Mehta and W. M. Worek, Analysis of Refraction Errors for Interferometric Measurements in Multicomponent Systems, *Appl. Opt.* vol. 23, pp. 928–933, 1984.
26. B. R. Ruddick and T. G. Shirtcliffe, Data for Double-Diffusers: Physical Properties of Aqueous Salt Solutions, *Deep Sea Res.* vol. 26A, pp. 775–787, 1992.
27. C. S. Virkam and W. K. Witherow, Critical Needs of Fringe-Order Accuracies in Two-Color Holographic Interferometry, *Exp. Mech.*, vol. 74, pp. 74–77, 1992.
28. Y. M. Chen and C. K. Liu, Time Dependent Double-Diffusive Convection due to Salt-Stratified Fluid Layer with Differential Heating in an Inclined Cavity, *Int. J. Heat Mass Transfer*, vol. 40, pp. 711–725, 1997.
29. S. L. Lee, Weighting Function Scheme and Its Application on Multidimensional Conservation Equations, *Int. J. Heat Mass Transfer*, vol. 32, pp. 2065–2073, 1989.
30. S. L. Lee and R. Y. Tzong, Artificial Pressure for Pressure Linked Equation, *Int. J. Heat Mass Transfer*, vol. 35, pp. 2705–2716, 1992.